J. Fluid Mech. (2019), *vol.* 873, *pp.* 459–474.
doi:10.1017/jfm.2019.425

Kinetic energy spectra and flux in turbulent phase-separating symmetric binary-fluid mixtures

Prasad Perlekar†

TIFR Centre for Interdisciplinary Sciences, Tata Institute of Fundamental Research, Hyderabad-500107, India

(Received 29 November 2018; revised 22 May 2019; accepted 22 May 2019; first published online 24 June 2019)

We conduct direct numerical simulations (DNS) of the Cahn–Hilliard–Navier–Stokes (CHNS) equations to investigate the statistical properties of a turbulent phase-separating symmetric binary-fluid mixture. Turbulence causes an arrest of the phase separation which leads to the formation of a statistically steady emulsion. We characterise turbulent velocity fluctuations in an emulsion for different values of the Reynolds number and the Weber number. Our scale-by-scale kinetic energy budget analysis shows that the interfacial terms in the CHNS equations provide an alternative route for the kinetic energy transfer. By studying the probability distribution function (p.d.f.) of the energy dissipation rate, the vorticity magnitude and the joint-p.d.f. of the velocity-gradient invariants we show that the statistics of the turbulent fluctuations do not change with the Weber number.

Key words: breakup/coalescence, isotropic turbulence, turbulence simulation

1. Introduction

Below the consolute temperature, a symmetric binary mixture with a spatially homogeneous composition spontaneously phase separates forming domains of individual phases via the process of spinodal decomposition, see e.g. the books Chaikin & Lubensky (1998) and Goldenfeld (2005). During the dynamics, individual domains merge and coarsen to form even larger domains until a final configuration is reached wherein two single-component domains separated by an interface are formed. The exact mechanism of domain growth depends on the interplay of viscous, inertial and surface tension forces (Lifshitz & Slyozov 1961; Siggia 1979; Furukawa 1985; Bray 1994; Kendon 2000; Kendon *et al.* 2001; Puri 2009; Datt, Thampi & Govindarajan 2015; Cates & Tjhung 2018).

The presence of external stirring such as shear or turbulent mixing counteracts the phase separation by breaking the coarsening domains to form a statistically stationary emulsion. In the presence of an external shear (with rate $\dot{\gamma}$), the size of a typical domain D in an emulsion state can be estimated by the balance of shear stress $\rho\nu\dot{\gamma}$

† Email address for correspondence: perlekar@tifrh.res.in

with the capillary force density σ/D which gives $D \sim \sigma/\rho\nu\dot{\gamma}$ (Hashimoto *et al.* 1995). Here ρ is the density, ν is the kinematic viscosity and σ is the surface tension of the emulsion. Although both experiments (Onuki 2002) and numerical simulations (Stansell *et al.* 2006; Stratford *et al.* 2007; Cates & Tjhung 2018) confirm the formation of an emulsion state, the domain size shows different scaling with shear rate in the directions perpendicular and parallel to the shear (Stansell *et al.* 2006; Stratford *et al.* 2007; Cates & Tjhung 2018).

The situation is much more tractable when the binary-fluid mixture emulsion is formed by external stirring that generates homogeneous isotropic turbulence (HIT). Because of the isotropy of the flow, a single length scale characterises the domain size. The average domain size D of such an emulsion can be estimated by a balance of inertial stress $(\rho(\delta_D U)^2)$ with the capillary force density (σ/D) (Hinze 1955), where $\delta_D U$ is the typical velocity difference across the domain. Using $\delta_D U \sim D^{1/3}\epsilon_{inj}^{1/3}$ (Kolmogorov 1941; Frisch 1996; Pandit, Perlekar & Ray 2009), where ϵ_{inj} is the energy dissipation rate, provides an estimate for the average domain size as $D \sim (\rho/\sigma)^{-3/5}\epsilon_{inj}^{-2/5}$. Early experiments (Pine *et al.* 1984; Easwar 1992) indicated an arrest of the phase-separation process in the presence of HIT. This was theoretically understood using eddy diffusivity arguments by Aronovitz & Nelson (1984). However, only recent numerical investigations using a multicomponent lattice–Boltzmann method in three dimensions (Perlekar *et al.* 2014) and direct numerical simulations (DNS) of Cahn–Hilliard–Navier–Stokes equations in two dimensions (Berti *et al.* 2005; Fan *et al.* 2016; Perlekar, Pal & Pandit 2017; Fan, Diamond & Chacon 2018) have been able to study emulsification by turbulence in symmetric binary-fluid mixtures. Surprisingly, unlike shear flows, here the numerically calculated domain size is in excellent agreement with Hinze's prediction in both two and three dimensions.

In two dimensions, Perlekar *et al.* (2017) show that the inverse energy cascade and the corresponding energy flux are blocked at a wavenumber corresponding to the domain size D. In three dimensions, numerical investigations (Kendon *et al.* 2001; Perlekar *et al.* 2014) show that for a binary-fluid mixture the energy content in the inertial range is suppressed in comparison to a single-component fluid at the same Reynolds number. However, an understanding of the underlying energy transfer mechanisms in three dimensions remains unclear.

In this paper, we conduct DNS to investigate the energy transfer mechanisms and the statistical properties of the velocity fluctuations in a stirred three-dimensional symmetric binary-fluid mixture. Our main findings are: (i) external stirring arrests phase separation (coarsening); (ii) our scale-by-scale analysis reveals that interfaces provide an alternative route for energy transfer and dissipation; (iii) for identical Reynolds number, a single-component fluid and a binary-fluid mixture have the same small-scale statistics.

The rest of the paper is organised as follows. We present the equations and the numerical method that we use in § 2. In §§ 3.1–3.3 we derive the equations for the total energy and the scale-by-scale kinetic energy budget, and present our numerical findings. In § 4 we investigate the small-scale statistics of the vorticity magnitude and the energy dissipation rate. We conclude in § 5.

2. Equations and direct numerical simulation (DNS)

We model a phase-separating symmetric binary-fluid mixture by using the Cahn–Hilliard–Navier–Stokes (CHNS) or Model-H equations (Cahn 1968; Hohenburg

& Halperin 1977; Celani *et al.* 2009; Yue, Zhou & Feng 2010; Magaletti *et al.* 2013; Fan *et al.* 2016; Pandit *et al.* 2017; Perlekar *et al.* 2017):

$$(\partial_t + \boldsymbol{u}\cdot\boldsymbol{\nabla})\boldsymbol{u} = \nu\nabla^2\boldsymbol{u} - \boldsymbol{\nabla}P + \Lambda\phi\boldsymbol{\nabla}\nabla^2\phi + \boldsymbol{f}, \tag{2.1}$$

$$(\partial_t + \boldsymbol{u}\cdot\boldsymbol{\nabla})\phi = M\nabla^2\mu, \tag{2.2}$$

$$\mu \equiv \Lambda\left(\frac{-\phi+\phi^3}{\xi^2} - \nabla^2\phi\right), \tag{2.3}$$

$$\boldsymbol{\nabla}\cdot\boldsymbol{u} = 0. \tag{2.4}$$

Here $\phi, \boldsymbol{u}$ and P are the Cahn–Hilliard order parameter, the velocity and the pressure field at position $\boldsymbol{x}$ and time t, ν is the kinematic viscosity, M is the mobility, ξ controls the width of the interface between the two phases, Λ is the mixing energy density, the order-parameter diffusivity $\kappa \equiv M\Lambda/\xi^2$, the surface tension $\sigma \equiv 2\sqrt{2}/3(\Lambda/\xi)$ and $\boldsymbol{f}$ is the external forcing that generates turbulence. The order parameter takes positive values in one phase and negative in the other. For simplicity, we assume the density ($\rho = 1$), the viscosity η and the mobility M to be independent of ϕ and the same for the two phases (in the lattice–Boltzmann simulations of Perlekar *et al.* (2014), mobility depends on ϕ). The local vorticity $\boldsymbol{\omega} \equiv \boldsymbol{\nabla}\times\boldsymbol{u}$. Note that the pressure P also contains contributions due to the gradient terms in ϕ. We use a cubic domain with each side of length $\mathcal{L} = 2\pi$ and discretise it with N^3 collocation points. We employ periodic boundary conditions. Equations (2.1) and (2.2) are numerically integrated using a pseudo-spectral method with 1/2-dealiasing and time marching is done using an exponential Adams–Bashforth scheme (Cox & Matthews 2002). A large-scale forcing $\hat{\boldsymbol{f}}_{\boldsymbol{k}} = f_0\hat{\boldsymbol{u}}_k/\sum_{k=1,2}|\hat{\boldsymbol{u}}_k|^2$, where the caret indicates Fourier transform, with $|\boldsymbol{k}| \leqslant 2$ ensures a constant energy injection rate $\epsilon_{inj} = f_0$.

2.1. *Interface width ξ and mobility M*

For an incompressible binary-fluid mixture such as 3-methylpentane-nitroethane (3MP-NE), $\xi \approx 10^{-9}$ m, $\sigma \approx 10^{-2}$ kg s^{-2} and the diffusivity κ is expected to be within an order of its value above the consolute temperature, i.e. $\kappa \leqslant 10^{-12}$ m^2 s^{-1} (Wims *et al.* 1970; Aronovitz & Nelson 1984; Pine *et al.* 1984). Substituting these values in the definition of κ, we get an estimate for mobility $M = \kappa\xi^2/\Lambda \sim 10^{-20}$ kg^{-1} m^3 s.

It is numerically prohibitive to use such vanishingly small ξ and M in CHNS equations. However, using an asymptotic analysis Magaletti *et al.* (2013) found that for $\xi \ll \mathcal{L}$ and with $M \propto \mathcal{L}\xi^3/(\Lambda\tau_{\mathcal{L}})$ (or equivalently $\kappa \propto \mathcal{L}\xi/\tau_{\mathcal{L}}$), the solution of the CHNS equations is consistent with the 'sharp-interface' limit ($\xi \to 0$ and $M \to 0$). Thus in all our numerical simulations we have used $\kappa \approx 2.5(\mathcal{L}/\tau_{\mathcal{L}})\xi \approx 10^{-2}$.

The flat-interface profile $\phi(\boldsymbol{x}) = \tanh(x/\sqrt{2}\xi)$ is an equilibrium solution of the CHNS equations. Following Jacqmin (1999), we define the interface width $w = 4.164\xi$ as the distance over which ϕ varies from -0.9 to 0.9. To have a fully resolved interface, in our direct numerical simulations we choose $\xi(\ll \mathcal{L})$ such that there are at least six grid points across the interface (Celani *et al.* 2009; Scarbolo *et al.* 2013). Thus for a given grid spacing $\delta x \equiv \mathcal{L}/N$, we set $\xi = 6\delta x/4.164$.

3. Results

The energy injection based Reynolds number $Re \equiv \sqrt{\epsilon_{inj}^{1/3}\mathcal{L}^{4/3}/\nu}$ and Weber number $We \equiv \epsilon_{inj}^{2/3}\mathcal{L}^{5/3}/\sigma$ characterise the turbulence intensity of the flow. Table 1 summarises

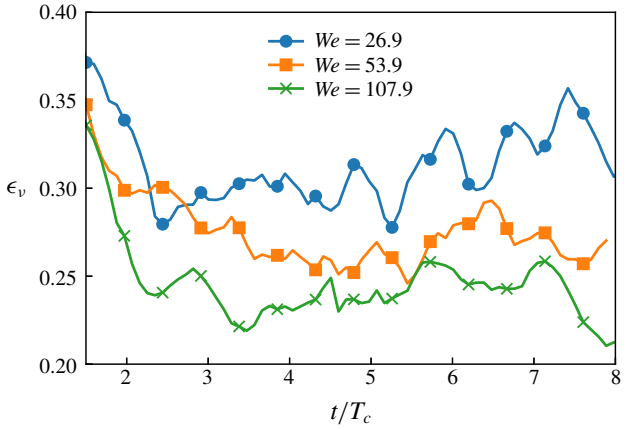

FIGURE 1. (Colour online) Time evolution of the viscous dissipation ϵ_v for a fixed $Re = 96$ and different We (runs SP21, SP23, and SP24).

	N	ν	$\xi(\times10^{-2})$	κ	$\sigma(\times10^{-1})$	Re	We	ϵ_{inj}	$\epsilon_v(\times10^{-1})$	$\epsilon_\mu(\times10^{-1})$
NS1	256	10^{-3}	—	—	—	65	—	0.05	0.05	—
SP11	256	10^{-3}	3.76	10^{-2}	2.51	65	11.6	0.05	0.33	0.18
SP12	256	10^{-3}	3.76	10^{-2}	0.63	65	46.4	0.05	0.23	0.28
SP13	256	10^{-3}	3.76	10^{-2}	0.25	65	116.2	0.05	0.23	0.27
NS2	512	10^{-3}	—	—	—	96	—	0.5	0.5	—
SP21	512	10^{-3}	1.88	10^{-2}	5.02	96	26.9	0.5	3.10	1.90
SP22	512	10^{-3}	1.88	10^{-2}	3.76	96	35.9	0.5	2.90	2.15
SP23	512	10^{-3}	1.88	10^{-2}	2.50	96	53.9	0.5	2.67	2.35
SP24	512	10^{-3}	1.88	10^{-2}	1.25	96	107.9	0.5	2.39	2.55

TABLE 1. Parameters N, ν, ξ, κ, σ, Re, We, ϵ_{inj}, ϵ_v, and ϵ_μ for our binary-fluid DNS SP11-13 and SP21-24. The NS runs are the DNS studies conducted for single-component Navier–Stokes fluid with the same ν and ϵ_{inj} as the binary fluid.

the parameters that we use. We present a grid convergence study for our high-Re, high-We run (SP24) in the Appendix. All the simulations were time integrated up to $t \approx 8T_{\mathcal{L}}$ ($T_{\mathcal{L}} \equiv \epsilon_{inj}^{-1/3}\mathcal{L}^{2/3}$). We plot the time evolution of the viscous dissipation $\epsilon_v(t) = \nu \sum_k k^2|\hat{\boldsymbol{u}}_{\boldsymbol{k}}|^2$ in figure 1 and observe that a statistically steady state is attained for $t > 2.5T_{\mathcal{L}}$.

3.1. *Domain size and energy balance*

In figure 2 we plot representative snapshots of the steady-state order-parameter field ϕ for our runs SP21 ($Re = 96$, $We = 26.9$) and SP24 ($Re = 96$, $We = 107.9$). We observe that the domain size in the emulsion decreases with increasing We. From ϕ, we estimate the average domain size as

$$L_c = 2\pi \left\langle \frac{\sum_{\boldsymbol{k}} |\hat{\phi}_{\boldsymbol{k}}|^2}{\sum_{\boldsymbol{k}} k|\hat{\phi}_{\boldsymbol{k}}|^2} \right\rangle, \tag{3.1}$$

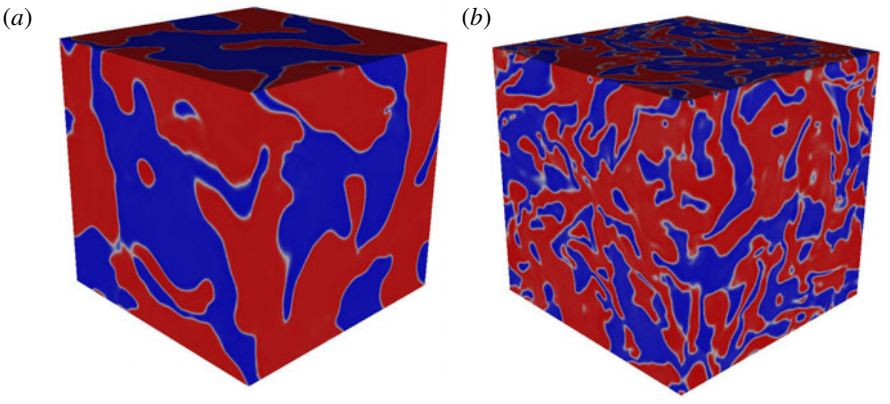

FIGURE 2. (Colour online) Pseudocolour plot of the order-parameter field ϕ for $Re = 96$, $We = 26.9$ (a) and for $Re = 96$, $We = 107.9$ (b). Regions with $\phi = 1(-1)$ are shown in red (blue). Average domain size decreases with increasing We.

where $k = \sqrt{\boldsymbol{k}\cdot\boldsymbol{k}}$ and angular brackets denote time averaging in the statistically steady state (Kendon *et al.* 2001; Perlekar *et al.* 2014, 2017; Fan *et al.* 2016). In figure 3(a) we present a plot of L_c versus $\epsilon_{inj}^2/\sigma^3$ for different values of Re and We (see table 1). We find the data to be in good agreement with Hinze's prediction for the average domain size in an emulsion $D \sim (\epsilon_{inj}^2/\sigma^3)^{-1/5}$.

Geometrically the average domain size can be obtained by measuring the inverse of the interfacial area $\mathcal{S}$ per unit volume (Furukawa 2000). We identify the interface as a region with $\phi = 0$ and use the 'GNU triangulation surface' (GTS) library (Popinet & Jones 2004) to evaluate steady-state $\mathcal{S}$. In the inset of figure 3(a) we show that $L_c \sim \mathcal{L}^3/\mathcal{S}$. Thus a unique length scale describes the domain size.

We next investigate how much of the energy injected ϵ_{inj} is dissipated by the viscosity ϵ_ν and how much is the contribution due to chemical potential ϵ_μ. Using (2.1) and (2.2), we obtain the following energy balance equation:

$$\partial_t \underbrace{\frac{1}{\mathcal{L}^3}\int \frac{|\boldsymbol{u}|^2}{2}\,\mathrm{d}\boldsymbol{x}}_{\mathcal{K}} + \partial_t \underbrace{\frac{1}{\mathcal{L}^3}\int \frac{\Lambda}{\xi^2}\left(-\frac{\phi^2}{2}+\frac{\phi^4}{4}+\frac{\xi^2}{2}|\nabla\phi|^2\right)\mathrm{d}\boldsymbol{x}}_{\mathcal{G}}$$
$$= -\underbrace{\frac{\nu}{\mathcal{L}^3}\int |\nabla u|^2\,\mathrm{d}\boldsymbol{x}}_{\epsilon_\nu} - \underbrace{\frac{M}{\mathcal{L}^3}\int |\nabla\mu|^2\,\mathrm{d}\boldsymbol{x}}_{\epsilon_\mu} + \underbrace{\frac{1}{\mathcal{L}^3}\int \boldsymbol{f}\cdot\boldsymbol{u}\,\mathrm{d}\boldsymbol{x}}_{\epsilon_{inj}}. \tag{3.2}$$

Here $\mathcal{K}$ is the kinetic energy, $\mathcal{G}$ is the free energy of mixing, ϵ_ν is the viscous energy dissipation, ϵ_μ is the dissipation because of the chemical potential (interfacial contribution due to breakup and merger of the domains) and ϵ_{inj} is the energy injected because of the external forcing. In the statistically steady state, $\langle\epsilon_{inj}\rangle \approx \langle\epsilon_\nu\rangle + \langle\epsilon_\mu\rangle$. In figure 3($b$,$c$) we show that for small We, the viscosity is the primary dissipation mechanism, $\langle\epsilon_\nu\rangle \gg \langle\epsilon_\mu\rangle$, whereas for large We average domain size reduces and the merger and breakup events increase thereby making the interfacial contribution more dominant, $\langle\epsilon_\mu\rangle > \langle\epsilon_\nu\rangle$. From (2.2), it is easy to show that in the steady state $\epsilon_\mu = \langle\int \boldsymbol{u}\cdot\phi\nabla\mu\,\mathrm{d}\boldsymbol{x}/\mathcal{L}^3\rangle$. Since $u \sim (\epsilon_{inj}\mathcal{L})^{1/3}$ and $\nabla\mu \sim \sigma/D^2$ (Bray 1994), we obtain

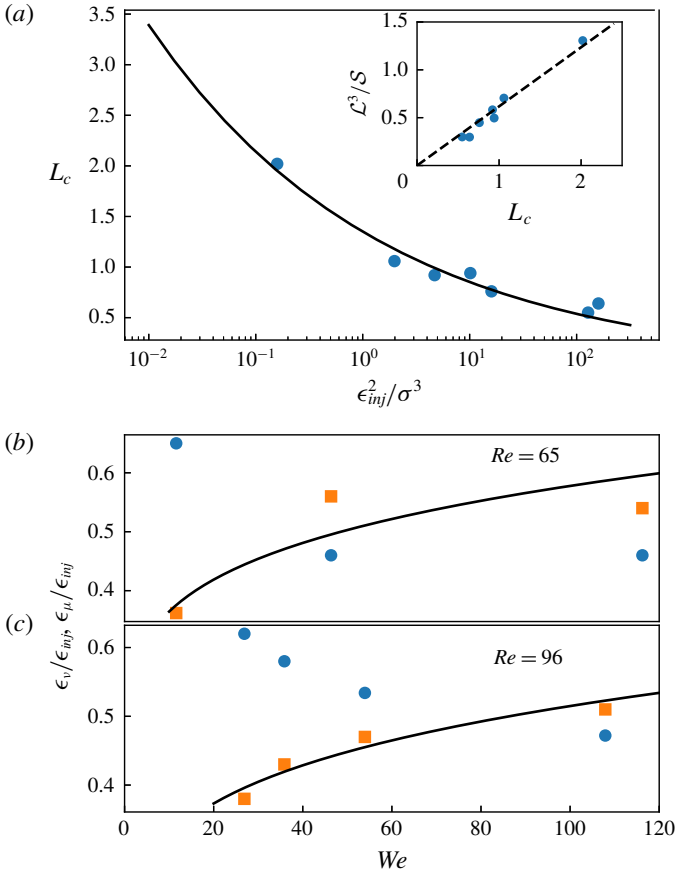

FIGURE 3. (Colour online) (*a*) Semi-log plot of the domain scale L_c versus $\epsilon_{inj}^2/\sigma^3$ (blue circle) and its comparison with the Hinze prediction for the domain scale ($D \sim (\epsilon_{inj}^2/\sigma^3)^{-1/5}$, black line). Inset: scatter plot of the domain scale L_c versus $\mathcal{L}^3/\mathcal{S}$ (blue circle); black dashed line is the linear fit $\mathcal{L}^3/S = 0.62L_c$. (*b*,*c*) $\epsilon_\nu/\epsilon_{inj}$ (blue circle) and $\epsilon_\mu/\epsilon_{inj}$ (orange square) with varying Weber number We for $Re = 65$ (runs `SP11-13`) and $Re = 96$ (runs `SP21-24`), respectively. Black line shows $\epsilon_\mu/\epsilon_{inj} \sim We^{1/5}$ scaling.

the prediction $\epsilon_\mu/\epsilon_{inj} \sim We^{1/5}$ which is in reasonable agreement with the results obtained from our DNS.

3.2. *Energy spectrum*

The steady-state energy spectrum is defined as (Vincent & Meneguzzi 1991)

$$E(k) = \frac{1}{2}\left\langle \sum_{k-1/2<k'\leqslant k+1/2} |\hat{\boldsymbol{u}}_{\boldsymbol{k}'}|^2 \right\rangle. \tag{3.3}$$

For high-Reynolds-number single-component turbulent flows, the energy spectrum shows Kolmogorov scaling $E(k) \sim k^{-5/3}$ in the inertial range (Kolmogorov 1941; Frisch

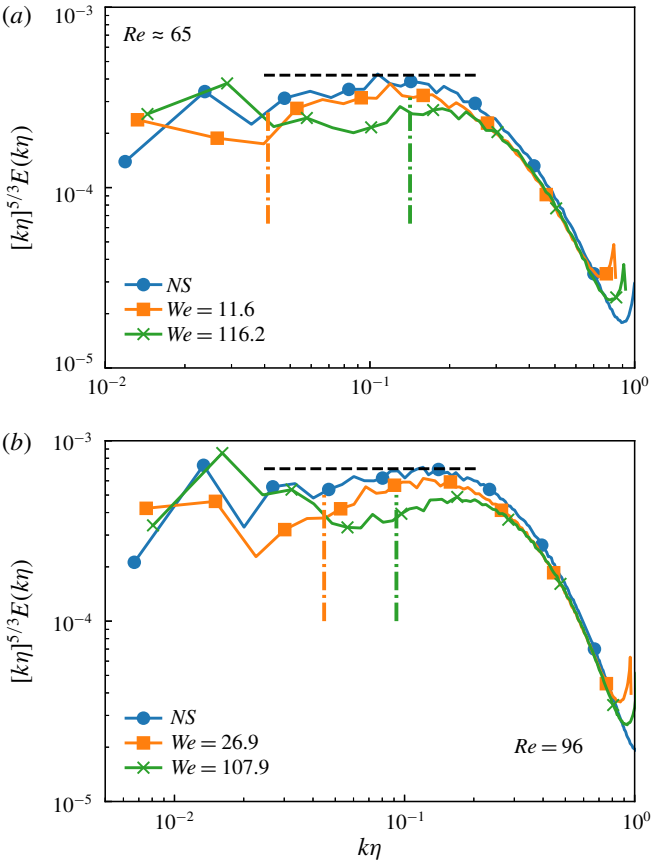

FIGURE 4. (Colour online) Energy spectrum for (*a*) $Re = 65$ and (*b*) $Re = 96$ for different values of We. The horizontal dashed line indicates Kolmogorov scaling and the vertical dash-dot lines indicate the wavenumber corresponding to the average domain size $2\pi/L_c$ in the emulsion. Here, $\eta = (\nu^3/\epsilon_\nu)^{1/4}$ is the viscous-dissipation scale.

1996). The energy spectrum obtained from our DNS runs `NS1` and `NS2` shows half a decade of scaling for $Re = 65$ and nearly a decade of scaling for $Re = 96$ (see figure 4).

We now investigate the energy spectrum for a turbulent binary-fluid mixture. It is important to note that our parameter choice ensures that the wavenumber corresponding to the interfacial width $k_w = 2\pi/w$ ($k_w\eta > 0.5$) lies beyond the inertial range.

For scales much larger and much smaller than the domain size L_c, we expect the statistical properties of the binary fluid to be same as the single-component fluid. In particular, we expect Kolmogorov scaling for scales much larger than the domain size but smaller than the injection scale ($2\pi/\ell_{inj} \ll k \ll 2\pi/L_c$). The energy spectrum should be modified for scales comparable to the domain size, $k \sim 2\pi/L_c$, because of redistribution and dissipation of energy due to breakup and merger of domains. Finally, for scales much smaller than the domain size but larger than the dissipation scale ($2\pi/L_c \ll k \ll 2\pi/\eta$) Kolmogorov scaling should be recovered. Unfortunately, because of the range of scales involved, it is computationally prohibitive to observe

all these different regimes in a single DNS. We, therefore, vary the We and Re to access different regimes discussed above.

For low Weber number ($We = 11.6$, $Re \approx 65$ and $We = 26.9$, $Re \approx 96$), the domain size $L_c \gg \eta$ and we observe that the energy spectrum follows its single-component counterpart and shows Kolmogorov scaling for $k > 2\pi/L_c$. For high Weber number ($We = 116.2$, $Re \approx 65$ and $We = 107.9$, $Re \approx 96$), the domain size $L_c \ll \ell_{inj}$. We find a reduction in the energy content around $k \approx 2\pi/L_c$ and it becomes comparable to the single-component spectrum for small k. This indicates a possibility that the Kolmogorov scaling is recovered for $k \ll 2\pi/L_c$. Clearly, numerical simulations with large scale separation and much higher spatial resolutions are required to investigate the recovery of Kolmogorov scaling for $2\pi/\ell_{inj} \ll k \ll 2\pi/L_c$.

3.3. *Scale-by-scale kinetic energy budget*

To investigate how the kinetic energy is distributed up to a given length scale ℓ (or a corresponding wavenumber $k = 2\pi/\ell$), we now derive the scale-by-scale energy budget equation. By multiplying the Fourier-transformed (2.1) with $\hat{\boldsymbol{u}}_{-\boldsymbol{k}}$, summing contributions up to wavenumber k, and then averaging over statistically steady state we obtain

$$\Pi(k) = -\mathcal{D}(k) - \Pi^{\phi}(k) + \mathcal{F}(k). \tag{3.4}$$

Here $\Pi(k) \equiv \langle \mathrm{Re}[\sum_{|\boldsymbol{m}|\leqslant k} \hat{\boldsymbol{u}}_{\boldsymbol{m}} \cdot (\widehat{\boldsymbol{u}\cdot\boldsymbol{\nabla}\boldsymbol{u}})_{-\boldsymbol{m}}]\rangle$ is the energy flux, $\Pi^{\phi} \equiv \Lambda \langle \mathrm{Re}[\sum_{|\boldsymbol{m}|\leqslant k} \hat{\boldsymbol{u}}_{\boldsymbol{m}} \cdot (\widehat{\phi\boldsymbol{\nabla}\nabla^2\phi})_{-\boldsymbol{m}}]\rangle$ is the cumulative flux of $(\boldsymbol{\nabla}\phi)^2$, $\mathcal{E}(k) \equiv \sum_{m\leqslant k} E(m)$ is the cumulative energy up to wavenumber k, $\mathcal{D}(k) \equiv \nu \sum_{m\leqslant k} m^2 E(m)$ is the cumulative dissipation up to wavenumber k and $\mathcal{F}(k) \equiv \langle \sum_{|\boldsymbol{m}|\leqslant k} \mathrm{Re}[\hat{\boldsymbol{u}}_{-\boldsymbol{m}}\hat{\boldsymbol{f}}_{\boldsymbol{m}}]\rangle$ is the cumulative energy injected. Note that for the largest wavenumber $k_{max} = N/4$, the scale-by-scale kinetic energy budget is the same as the kinetic energy balance because $\Pi(k_{max}) = 0$, $\mathcal{D}(k_{max}) = \epsilon_{\nu}$, $\Pi^{\phi}(k_{max}) = \epsilon_{\mu}$, and $\mathcal{F}(k_{max}) = \epsilon_{inj}$.

The plots in figure 5(*a*,*b*) show the scale-by-scale energy budget for $Re = 65$ and $Re = 96$ for a single-component fluid. The energy is injected at large scales by forcing $\mathcal{F}(k)$ and is dissipated by viscosity at small scales. The Navier–Stokes nonlinearity transfers the kinetic energy in the inertial range while keeping its flux $\Pi(k)$ constant. For our high $Re = 96$ run `NS2`, we observe a nearly constant $\Pi(k) \sim \epsilon_{inj}$ for $2 \leqslant k \leqslant 10$ which manifests as an extended inertial range in the energy spectrum (see figure 4*b*).

We now show that for the binary-fluid case, the presence of emulsion domains dramatically alters the energy transfer mechanism. Firstly, for small We we find that for large k ($\gg 2\pi/L_c$) the viscous dissipation $\mathcal{D}(k)$ is larger than the contribution due to interfacial flux $\Pi^{\phi}(k)$ (figure 5*c*,*d*) whereas it is the opposite for high We (figure 5*e*,*f*). Secondly, the interfacial flux $\Pi^{\phi}(k)$ first increases up to a wavenumber corresponding to the arrest scale $k_c \approx 2\pi/L_c$. Above $k > k_c$, $\Pi^{\phi}(k)$ decreases until large k where it is equal to ϵ_{μ}. This indicates that the interface undulations absorb kinetic energy $\sim \Pi^{\phi}(k_c)$ from large scales. However only part of it, ϵ_{μ}, is dissipated and the excess energy $\sim \Pi^{\phi}(k_c) - \epsilon_{\mu}$ is redistributed among wavenumbers $k > k_c$. Finally, the contribution because of the kinetic energy flux $\Pi(k)$ is nearly halved in comparison to its single-component-fluid counterpart. Consistent with the discussion in the previous section, for $k > k_c$ we find a small range where $\Pi(k) \sim$ constant for $k > k_c$ (see figure 5). Note that in figure 5(*e*) (run `SP13`, $Re = 65$, and $We = 116.2$) we do

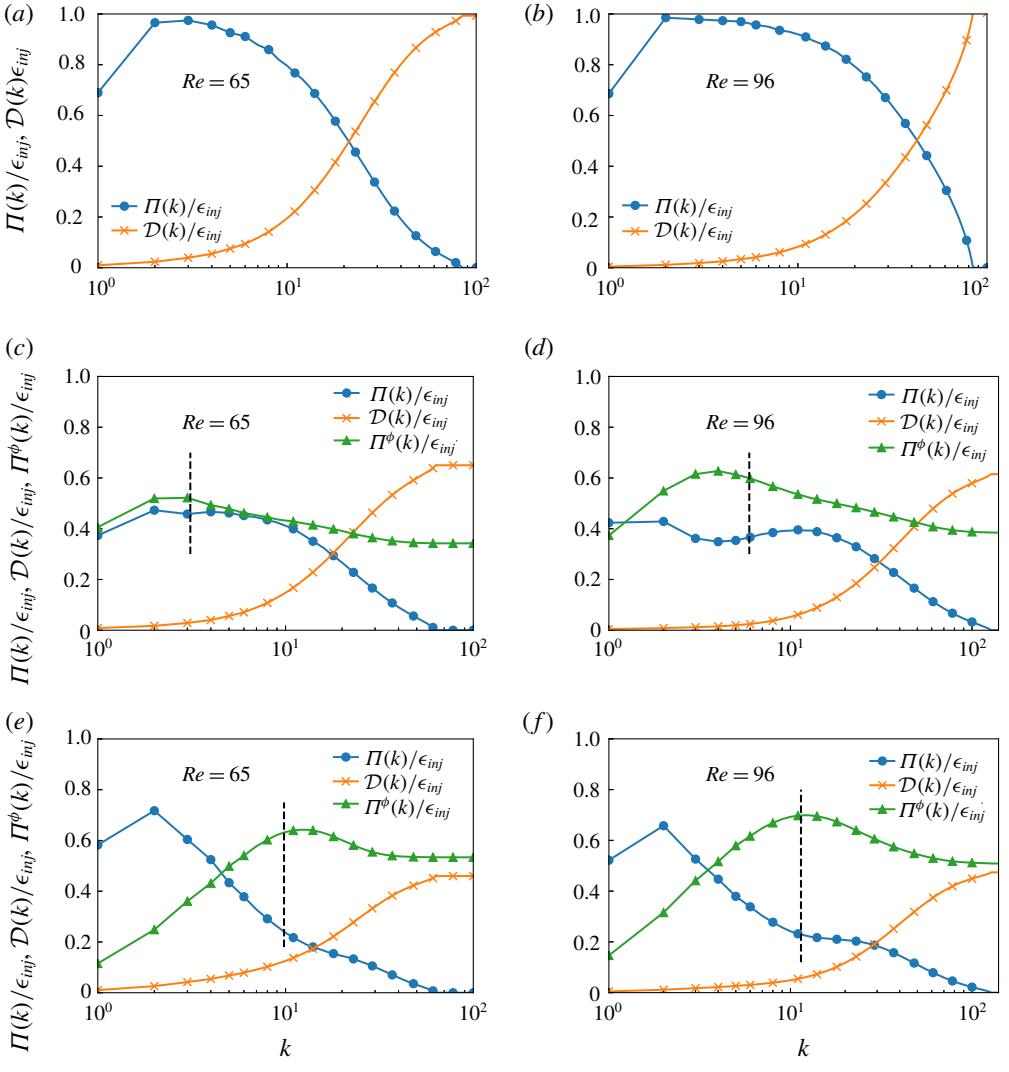

FIGURE 5. (Colour online) Energy flux for (*a*) $Re = 65$ (run `NS1`), (*b*) $Re = 96$ (run `NS2`), (*c*) $We \approx 11.6$, $Re \approx 65$ (run `SP11`), (*d*) $We \approx 26.9$, $Re \approx 96$ (run `SP21`), (*e*) $We \approx 116.2$, $Re \approx 65$ (run `SP13`), and (*f*) $We \approx 107.9$, $Re \approx 96$ (run `SP24`). The dashed vertical line indicate the wavenumber corresponding to the average domain size $2\pi/L_c$.

not observe a plateau region in $\Pi(k)$ due to lack of scale separation (the contribution due to viscous dissipation is comparable to the energy flux around $k = 2\pi/L_c$).

For $k < k_c$ we find that $\Pi(k)$ decreases with increasing k and balances interfacial flux $\Pi^{\phi}(k)$. Indeed, much larger scale separation is required to verify if the Kolmogorov scaling is recovered for $2\pi/\ell_{inj} \ll k \ll k_c$. Nevertheless, our study clearly shows that the presence of an interface opens up an additional mechanism for transferring kinetic energy from large scales to scales smaller than the average size of a domain in the emulsion.

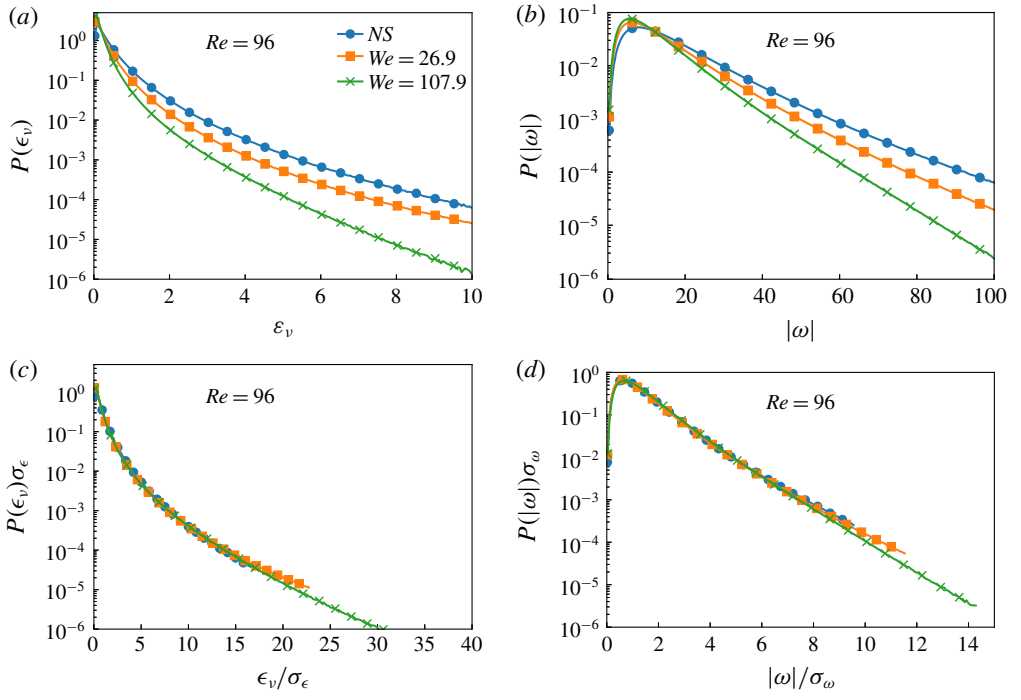

FIGURE 6. (Colour online) (*a*,*b*) Probability distribution function of the energy dissipation rate $P(\epsilon_\nu)$ versus ϵ_ν and the magnitude of the vorticity $P(|\omega|)$ versus $|\omega|$ for different *We*. (*c*,*d*) Normalised p.d.f.s $P(\epsilon_\nu)\sigma_\epsilon$ and $P(|\omega|)\sigma_\omega$ for different *We*. We fix $Re = 96$ (runs `SP21`, `SP24`). For comparison we also plot the corresponding p.d.f. for the pure fluid (run `NS2`).

4. Small-scale structures

We now investigate whether the different kinetic energy transfer mechanism in binary-fluid turbulence also alters the small-scale structures. In figure 6(*a*,*b*) we plot the statistics of the local viscous energy dissipation $\epsilon_{loc} = \nu \sum_{i,j} (\partial_i u_j + \partial_j u_i)^2/2$ and the magnitude of the vorticity field $|\boldsymbol{\omega}| = \sqrt{\boldsymbol{\omega} \cdot \boldsymbol{\omega}}$ for a binary-fluid mixture and compare it with a single-component fluid at the same *Re*. We observe a reduction in the events with large values of ϵ_{loc} and $|\boldsymbol{\omega}|$ on increasing *We*. However, the probability distribution functions (p.d.f.s) overlap when normalised by their standard deviations. Thus the small-scale statistics remains the same as that of a single-component turbulent fluid.

To investigate the flow structures, in figure 7 we plot the iso-vorticity contours for a turbulent binary mixture as well as turbulence in pure fluid and overlay the $\phi = 0$ contours on them to highlight the emulsion domains. For the single-component fluid, consistent with earlier studies (Ishihara, Gotoh & Kaneda 2009; Pandit *et al.* 2009), we observe tubular structures. For the case of a binary mixture, as shown earlier, smaller domains (more interfacial area) are formed as we increase *We*. Also, near the interfacial region vorticity appears to be concentrated. Thus the interface undulations also generate flow structures whose statistics are similar to that of turbulence in a single-component fluid.

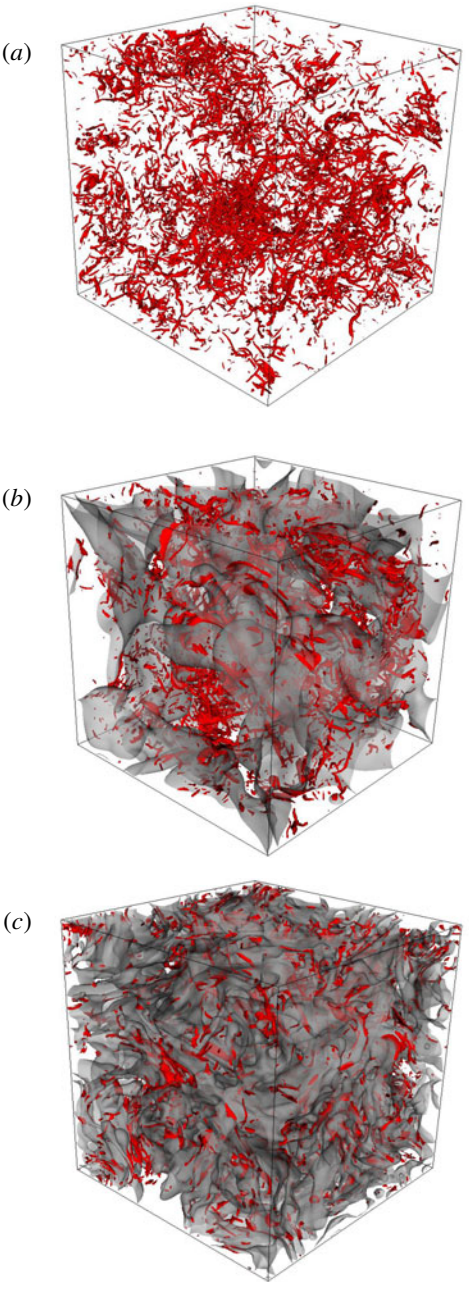

FIGURE 7. (Colour online) Representative steady-state iso-contour plots of the vorticity magnitude $|\omega|$ for $|\omega| = |\bar{\omega}| + 6\sigma_\omega$, where the overbar denotes spatial averaging. (*a*) Pure fluid with $|\omega| = 1.123$ (run NS2), (*b*) a turbulent binary mixture with $We = 26.9$ with $|\omega| = 0.93$ (run SP21) and (*c*) $We = 107.9$ with $|\omega| = 0.76$ (run SP22). For the binary-mixture plots we also overlay the iso-contour of the order parameter ϕ for $\phi = 0$ to highlight the interface.

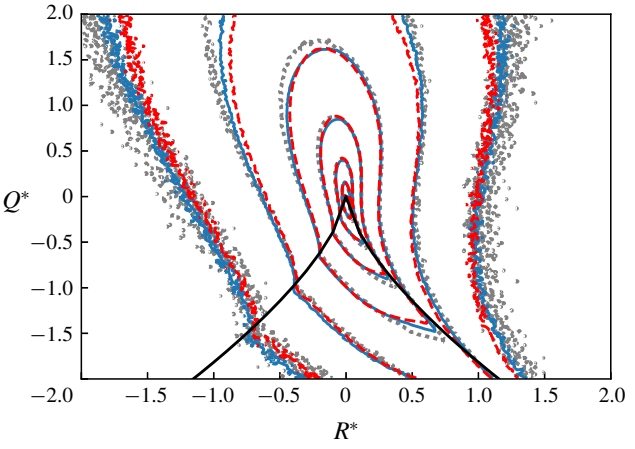

FIGURE 8. (Colour online) Contour plots of the joint p.d.f. $P(R^*, Q^*)$ for pure-fluid turbulence (grey dots, run NS2) and binary-fluid turbulence with $We = 26.9$ (blue line, run SP21), $We = 107.9$ (red dashed line, run SP24). Here $R^* = \nu^{3/2}R/\epsilon_\nu^{3/2}$ and $Q^* = \nu Q/\epsilon_\nu$. Contours are logarithmically spaced and separated by factors of 10. For all We, the value of the outermost contour is 10^{-4}. The black curve is the $\Delta = 0$ line that demarcates regions with vortical $\Delta > 0$ or strain $\Delta < 0$ dominated flow structures.

The local flow structures as observed by a Lagrangian fluid parcel in a turbulent flow can be quantified by the invariants $R \equiv -\mathrm{Tr}(\boldsymbol{A}^2)/2$ and $Q \equiv -\mathrm{Tr}(\boldsymbol{A}^3)/3$ of the velocity gradient tensor $\boldsymbol{A} \equiv \boldsymbol{\nabla u}$ (Perry & Chong 1987; Cantwell 1992). The joint p.d.f. $P(R, Q)$ provides an understanding of the typical structures encountered in a turbulent flow. The discriminant $\Delta \equiv 27Q^3/4 + R^2$ demarcates the regions dominated by vortices ($\Delta > 0$) from those that are dominated by strain ($\Delta < 0$). To quantify whether the structures formed in pure-fluid turbulence are similar to or different from a turbulent binary mixture, in figure 8 we plot the joint p.d.f. $P(R, Q)$ for the pure-fluid turbulence as well as binary-fluid turbulence with $Re = 96$ and $We = 26.9, 107.9$. Although the qualitative features remain the same we observe a small but systematic shrinkage of the iso-contour lines with increasing We.

5. Conclusions

We investigated turbulence in a stirred phase-separated symmetric binary-fluid mixture. Our study reveals that external stirring leads to the formation of a statistically steady emulsion. The Hinze scale provides an estimate for the average domain size. For a binary-fluid mixture, in comparison to a single-component fluid, kinetic energy content is reduced for length scales comparable to the domain size. We show that this is because the presence of interfaces opens up an alternative kinetic energy transfer mechanism. Emulsion domains absorb kinetic energy at scales comparable to the Hinze scale, dissipate part of it and redistribute the rest to small scales. Surprisingly, even with an alternative energy transfer mechanism, we do not find any qualitative change in the statistics of small-scale structures.

Our results bear a striking similarity with those of polymeric turbulence (Perlekar, Mitra & Pandit 2006, 2010; Valente, Silva & Pinho 2014). There also the presence of polymers modifies the energy transfer in the inertial range. This similarity could be

attributed to a close correspondence between the CHNS equations and the equations for uniaxial polymers (Balkovsky, Fouxon & Lebedev 2001). However, a crucial difference is that the typical size of the polymer is in the dissipation range and they are homogeneously distributed throughout the flow, whereas the size of binary-fluid domains lies within the inertial range (Aronovitz & Nelson 1984; Perlekar *et al.* 2014; Fan *et al.* 2016).

Acknowledgements

We thank M. M. Bandi, M. Barma, D. Mitra, and F. Toschi for their comments and suggestions.

Appendix. Optimal grid resolution

To correctly capture the dynamics of a turbulent binary-fluid mixture it is essential to have both the interface ξ as well as the dissipation range well-resolved. Thus to estimate optimal grid resolution, we conduct DNS for our largest-(Re, We) run SP24 with fixed length $\mathcal{L}$ and varying N. Based on the criterion discussed in § 2.1, it is straightforward to show that for $\xi = 1.88 \times 10^{-2}$, a grid resolution with $N \geqslant 482$ is needed to have a well-resolved interface. We perform DNS with $N = 256, 320, 512$ and 1024 and monitor the steady-state energy dissipation rate and the energy spectrum. We initialise the $N = 1024$ configuration from an $N = 512$ steady-state configuration and further time-integrate it for $2\mathcal{T}_{\mathcal{L}}$.

In figure 9(*a–d*) we plot representative snapshots of the steady-state order-parameter field ϕ for different grid resolution. In all the cases the average domain size is correctly captured. However at the lowest grid resolution ($N = 256$), since interface is not well-resolved, we observe the presence of small-scale fluctuations. The viscous dissipation shows similar evolution for different grid resolutions (see figure 9*e*). Indeed the steady-state viscous dissipation ϵ_ν is comparable (see table 2) for all the cases. Next, in figure 9(*f*) we present a comparison of the steady-state energy spectrum $E(k\eta)$ for different N. Although the inertial-range behaviour is identical for all the runs, at low grid resolutions ($N = 256$ and $N = 320$) we see a pile-up of energy at large k which is a hallmark of under-resolved spectral simulations (Canuto *et al.* 1988). The energy spectrum for high-resolution runs ($N = 512$ and $N = 1024$) is well-resolved and indistinguishable over the entire range. Since it is desirable to have a well-resolved energy spectrum and also long time integration, we conclude that $N = 512$ provides an optimal grid resolution for $Re = 96$. A similar study reveals that for $Re = 65$, $N = 256$ is sufficient.

N	ϵ_ν
256	2.49×10^{-1}
320	2.40×10^{-1}
512	2.39×10^{-1}
1024	2.41×10^{-1}

TABLE 2. Steady-state value of the viscous dissipation ϵ_ν with different grid resolutions N. The other parameter values are the same as our binary-fluid DNS SP24 (see table 1).

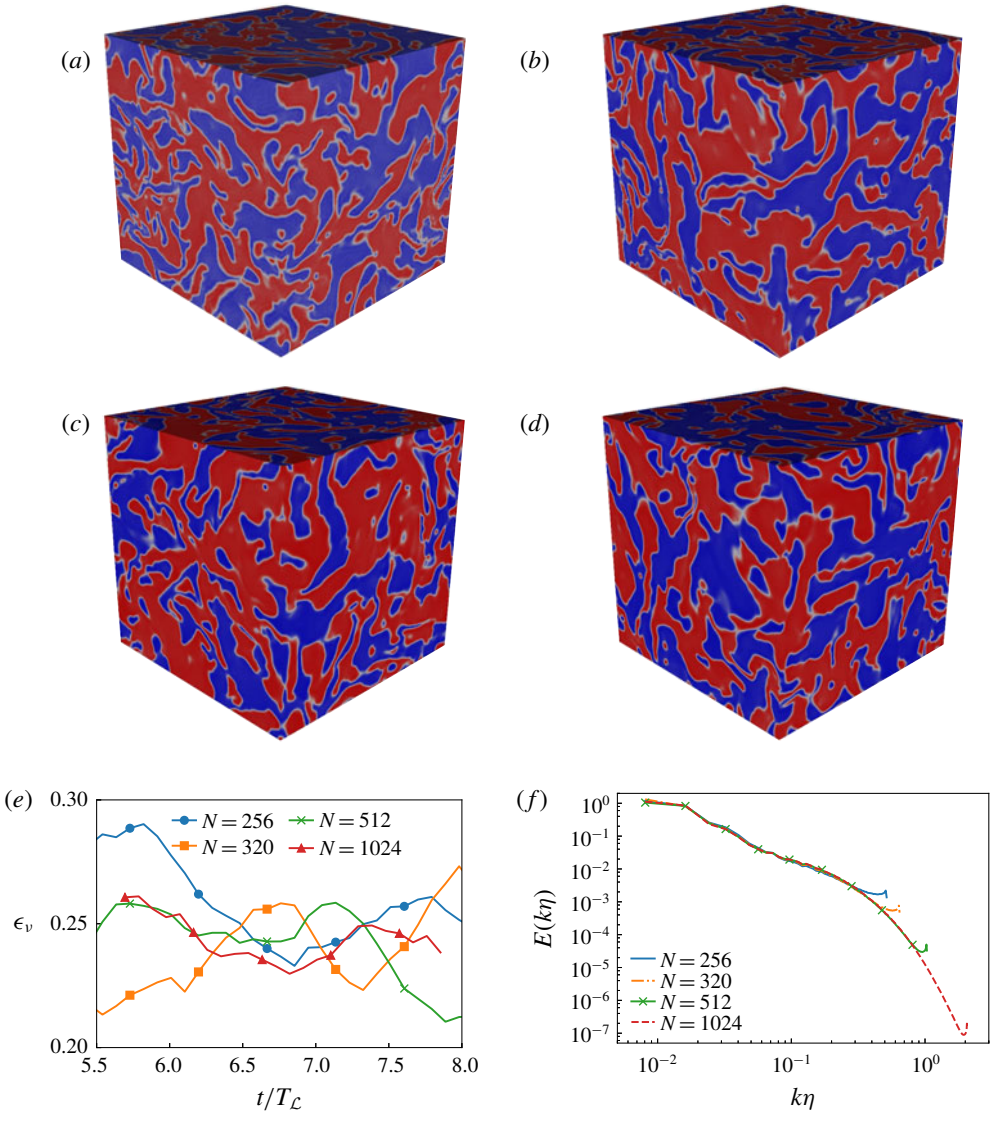

FIGURE 9. (Colour online) Grid convergence test for run SP24 ($Re = 96$, $We = 107.9$). Pseudocolour plot of the order-parameter field ϕ with increasing grid resolution: (*a*) $N = 256$, (*b*) $N = 320$, (*c*) $N = 512$ and (*d*) $N = 1024$; (*e*) time evolution of the viscous dissipation ϵ_ν and (*f*) steady-state energy spectrum $E(k)$ versus k.

REFERENCES

ARONOVITZ, J. A. & NELSON, D. R. 1984 Turbulence in phase-separating binary mixtures. *Phys. Rev.* A **29**, 2012–2016.

BALKOVSKY, E., FOUXON, A. & LEBEDEV, V. 2001 Turbulence in polymer solutions. *Phys. Rev.* E **64**, 056301.

BERTI, S., BOFFETTA, G., CENCINI, M. & VULPIANI, A. 2005 Turbulence and coarsening in active and passive binary mixtures. *Phys. Rev. Lett.* **95**, 224501.

BRAY, A. J. 1994 Theory of phase-ordering kinetics. *Adv. Phys.* **43**, 357–459.

CAHN, J. 1968 Spinodal decomposition. *Trans. Metall. Soc. AIME* **242**, 166–180.

CANTWELL, B. J. 1992 Exact solution of a restricted Euler equation for the velocity gradient tensor. *Phys. Fluids* A **4**, 782–793.

CANUTO, C., HUSSAINI, M. Y., QUARTERONI, A. & ZANG, T. A. 1988 *Spectral Methods in Fluid Dynamics*. Springer.

CATES, M. E. & TJHUNG, E. 2018 Theories of binary fluid mixtures: from phase-separation kinetics to active emulsions. *J. Fluid Mech.* **836**, 1–68.

CELANI, A., MAZZINO, A., MURATORE-GINANNESCHI, P. & VOZELLA, L. 2009 Phase-field model for the Rayleigh–Taylor instability of immisible fluids. *J. Fluid Mech.* **622**, 115–134.

CHAIKIN, P. M. & LUBENSKY, T. C. 1998 *Principles of Condensed Matter Physics*. Cambridge University Press.

COX, S. M. & MATTHEWS, P. C. 2002 Exponential time differencing for stiff systems. *J. Comput. Phys.* **176**, 430–455.

DATT, C., THAMPI, S. P. & GOVINDARAJAN, R. 2015 Morphological evolution of domains in spinodal decomposition. *Phys. Rev.* E **91**, 010101.

EASWAR, N. 1992 Effect of continuous stirring on off-critical and critical samples of a phase-separating binary liquid mixture. *Phys. Rev. Lett.* **68**, 186–189.

FAN, X., DIAMOND, P. H. & CHACON, L. 2018 Chns: a case study of turbulence in elastic media. *Phys. Plasmas* **25**, 055702.

FAN, X., DIAMOND, P. H., CAHCON, L. & HUI, L. 2016 Cascades and spectra of a turbulent spinodal decomposition in two-dimensional symmetric binary liquid mixtures. *Phys. Rev. Fluids* **1**, 054403.

FRISCH, U. 1996 *Turbulence the Legacy of A.N. Kolmogorov*. Cambridge University Press.

FURUKAWA, H. 1985 Effect of inertia on droplet growth in a fluid. *Phys. Rev.* A **31**, 1103–1108.

FURUKAWA, H. 2000 Spinodal decomposition of two-dimensional fluid mixtures: a spectral analysis of droplet growth. *Phys. Rev.* E **61**, 1423–1431.

GOLDENFELD, N. 2005 *Lectures on Phase Transitions and the Renormalization Group*. Levant Books.

HASHIMOTO, T., MATSUZAKA, K., MOSES, E. & ONUKI, A. 1995 String phase in phase-separating fluids under shear flow. *Phys. Rev. Lett.* **74**, 126–129.

HINZE, J. O. 1955 Fundamentals of the hydrodynamic mechanism of splitting in dispersion processes. *AIChE J.* **1**, 289–295.

HOHENBURG, P. & HALPERIN, B. 1977 Theory of dynamic critical phenomena. *Rev. Mod. Phys.* **49**, 435–479.

ISHIHARA, T., GOTOH, T. & KANEDA, Y. 2009 Study of high-Reynolds number isotropic turbulence by direct numerical simulation. *Annu. Rev. Fluid Mech.* **41**, 165–180.

JACQMIN, D. 1999 Calculation of two-phase navier-stokes flows using phase-field modeling. *J. Comput. Phys.* **155**, 96–127.

KENDON, V. M. 2000 Scaling theory of three-dimensional spinodal turbulence. *Phys. Rev.* E **61**, R6071.

KENDON, V. M., CATES, M. E., PAGANOBARRAGA, I., DESPLAT, J. C. & BLADON, P. 2001 Inertial effects in three-dimensional spindoal decomposition of a symmetric binary fluid mixture: a lattice Boltzmann study. *J. Fluid Mech.* **440**, 147–203.

KOLMOGOROV, A. N. 1941 The local structure of turbulence in incompressible viscous fluid for very large Reynolds numbers. *Dokl. Akad. Nauk USSR* **30**, 9–13.

LIFSHITZ, I. M. & SLYOZOV, V. V. 1961 The kinetics of precipitation from supersaturated solid solutions. *J. Phys. Chem. Solids* **19**, 35–50.

MAGALETTI, F., PICANO, F., CHINAPPI, M., MARINO, L. & CASCIOLA, C. M. 2013 The sharp-interface limit of the Cahn–Hilliard/Navier–Stokes model for binary fluids. *J. Fluid Mech.* **714**, 95–126.

ONUKI, A. 2002 *Phase Transition Dynamics*. Cambridge University Press.

PANDIT, R., BANERJEE, D., BHATNAGAR, A., BRACHET, M., GUPTA, A., MITRA, D., PAL, N., PERLEKAR, P., RAY, S. S., SHUKLA, V. *et al.* 2017 An overview of the statistical properties

of two-dimensional turbulence in fluids with particles, conducting fluids, fluids with polymer additives, binary-fluid mixtures, and superfluids. *Phys. Fluids* **29**, 111112.

PANDIT, R., PERLEKAR, P. & RAY, S. S. 2009 Statistical properties of turbulence: an overview. *Pramana* **73**, 179–213.

PERLEKAR, P., BENZI, R., CLERCX, H. J. H., NELSON, D. R. & TOSCHI, F. 2014 Spinodal decomposition in homogeneous and isotropic turbulence. *Phys. Rev. Lett.* **112**, 014502.

PERLEKAR, P., MITRA, D. & PANDIT, R. 2006 Manifestations of drag reduction by polymer additives in decaying, homogeneous, isotropic turbulence. *Phys. Rev. Lett.* **97**, 264501.

PERLEKAR, P., MITRA, D. & PANDIT, R. 2010 Direct numerical simulations of statistically steady, homogeneous, isotropic fluid turbulence with polymer additives. *Phys. Rev.* E **82**, 066313.

PERLEKAR, P., PAL, N. & PANDIT, R. 2017 Two-dimensional turbulence in symmetric binary-fluid mixtures: coarsening arrest by the inverse cascade. *Sci. Rep.* **7**, 44589.

PERRY, A. E. & CHONG, M. S. 1987 A description of eddying motions and flow patterns using critical-point concepts. *Annu. Rev. Fluid Mech.* **19**, 125–155.

PINE, D. J., EASWAR, N., MAHER, J. V. & GOLDBURG, W. I. 1984 Turbulent suppression of spinodal decomposition. *Phys. Rev.* A **29**, 308–313.

POPINET, S. & JONES, T. 2004 Gts: Gnu triangulated surface library. http://gts.sourceforge.net.

PURI, S. 2009 Kinetics of phase transitions. In *Kinetics of Phase Transitions* (ed. S. Puri & V. Wadhawan), vol. 6, p. 437. CRC Press.

SCARBOLO, L., MOLIN, D., PERLEKAR, P., SBRAGAGLIA, M., SOLDATI, A. & TOSCHI, F. 2013 Unified framework for a side-by-side comparison of different multicomponent algorithms: lattice Boltzmann versus phase filed model. *J. Comput. Phys.* **234**, 263–279.

SIGGIA, E. D. 1979 Late stages of spinodal decomposition in binary mixtures. *Phys. Rev.* A **20**, 595–605.

STANSELL, P., STRATFORD, K., DESPLAT, J. C., ADHIKARI, R. & CATES, M. E. 2006 Nonequilibrium steady states in sheared binary fluids. *Phys. Rev. Lett.* **96**, 085701.

STRATFORD, K., DESPLAT, J. C., STANSELL, P. & CATES, M. E. 2007 Binary fluids under steady shear in three dimensions. *Phys. Rev.* E **76**, 030501(R).

VALENTE, P. C., SILVA, D. C. B. & PINHO, F. T. 2014 The effect of viscoelasticity on the turbulent kinetic energy cascade. *J. Fluid Mech.* **760**, 39–62.

VINCENT, A. & MENEGUZZI, M. 1991 The spatial structure and statistical properties of homogeneous turbulence. *J. Fluid. Mech.* **225**, 1–20.

WIMS, A. M., SENGERS, J. V., MCINTYRE, D. & SHERESHEFSKY, J. 1970 Interfacial tension of 3-methylpentane-nitroethane near the critical point. *J. Chem. Phys.* **52**, 3042–3049.

YUE, P., ZHOU, C. & FENG, J. J. 2010 Sharp-interface limit of the Cahn–Hilliard model for moving contact lines. *J. Fluid Mech.* **645**, 279–294.